Materials Science & Engineering A 763 (2019) 138143

Contents lists available at ScienceDirect

Materials Science & Engineering A

journal homepage: www.elsevier.com/locate/msea

Effects of alloying on deformation twinning in high entropy alloys

Wei Li[a,b], Haidong Fan[a,*], Jing Tang[a], Qingyuan Wang[a,**], Xu Zhang[c], Jaafar A. El-Awady[b]

[a] Department of Mechanics, Sichuan University, Chengdu, 610065, China
[b] Department of Mechanical Engineering, Whiting School of Engineering, The Johns Hopkins University, Baltimore, MD, 21218, USA
[c] Applied Mechanics and Structure Safety Key Laboratory of Sichuan Province, School of Mechanics and Engineering, Southwest Jiaotong University, Chengdu, 610031, China

ARTICLE INFO

Keywords:
High entropy alloys
Twin nucleation stress
Molecular dynamics
Nanocrystals
Atomic strain and stress

ABSTRACT

In the current work, molecular dynamics (MD) simulations were employed to model the compressive property of FCC (face centered cubic) $Al_{0.25}CoFeNiCu_{0.75}$ high entropy alloy (HEA) nanopillars. For comparison the binary, ternary and quaternary derivatives based on Ni–Cu–Fe–Co–Al system along with pure Ni were investigated. The twin nucleation and migration stress, atomic strain and stress and generalized planar faults energy (GPFE) of the compositions were calculated. The simulation results suggest that plastic deformation of all nanopillars is mediated by deformation twinning, but both the yield strength and flow stress decrease with the increase in the number of alloying elements, implying the decrease in the twin nucleation and migration stresses, respectively. The atomic strain and stress, increasing with the addition of alloying elements, provide direct evidences at atomic scale for the severe lattice distortion resulting in the decrease in stacking fault energy (SFE) and twin boundary energy as shown in the GPFE curves. The SFE of $Al_{0.25}CoFeNiCu_{0.75}$ HEA is 16mJ/m^2. The twinnability of the studied compositions also increases with the addition of alloying elements, so twinning deformation dominates in the current nanocrystals.

1. Introduction

Multi-principle element alloys (MPEAs), multi-element solid solution alloys, or more commonly known as high entropy alloys (HEAs), have received significant attention in recent years due to their superior properties for cryogenic and high temperature applications. These alloys are typically composed of five or more elements in nearly equiatomic concentration (e.g. 5%–35%) [1–3]. While the mixing entropy of an alloy increases with the increasing number of alloying elements, recent studies indicate that higher mixing entropy leads to a lower Gibbs free energy, and thus suppresses the formation of intermetallic compounds. Accordingly, stable solid solution phases, such as face-centered cubic (FCC) phase, body-centered cubic (BCC) phase and hexagonal closed packed (HCP) phase can be obtained [4,5].

In recent years, numerous studies have been conducted to investigate the microstructure and mechanical properties of different HEAs through both experiments and simulations. The common combination of compositions that have been extensively studied includes Al–Co–Cr–Cu–Fe–Ni HEA systems, where the Al atoms have the largest atomic radius, and thus the Al atomic concentration significantly influences the crystalline structure. With increasing Al content, the crystalline structure of $CuCoNiCrAl_xFe$ HEA changes from a single FCC phase into a duplex FCC/BCC phase and then BCC + B2 phase [1]. In addition, the hardness of these HEAs also increases monotonously with increasing Al concentration [1]. Furthermore, Co, Cu and Ni elements facilitates the generation of an FCC phase, while Al and Cr elements facilitate the generation of BCC phase. Thus, increasing the content of Cu and decreasing that of Al stabilizes the single FCC phase in the Al–Co–Cr–Cu–Fe–Ni HEA system [6]. Accordingly, $Al_{0.25}CoFeNiCu_{0.75}$ HEA has an FCC crystal structure, while $Al_{0.75}CoFeNiCu_{0.25}$ has a BCC structure [7].

In general, HEAs exhibit outstanding mechanical properties, e.g. high strength and hardness [8,9], excellent resistance to softening at high temperature, high wear resistance [10], exceptional ductility, damage tolerance and fracture toughness at very low temperatures [11]. The favorable cryogenic properties have been attributed to the high working hardening capability induced by transition from dislocation mediated plasticity to deformation induced nano-twinning [11]. Furthermore, at room temperature, nano-twinning was also observed at high strain levels [12] or during high pressure torsion deformation [13]. In these cases, the deformation induced nano-twinning is expected to contribute to the increased work hardening by

* Corresponding author.
** Corresponding author.
E-mail addresses: hfan85@scu.edu.cn (H. Fan), wangqy@scu.edu.cn (Q. Wang).

https://doi.org/10.1016/j.msea.2019.138143
Received 9 March 2019; Received in revised form 20 June 2019; Accepted 10 July 2019
Available online 11 July 2019
0921-5093/

introducing new interfaces in the materials that would impede dislocation slip [13]. When the stacking fault energy of an HEA is very low, twinning deformation would be favorable and play an important role in controlling the mechanical properties.

Molecular dynamics (MD) simulations can provide an effective tool to characterize the microstructure and deformation mechanisms in HEAs, which are difficult to quantify experimentally [14]. However, to date, only a limited number of MD studies have been performed on HEAs. The plastic deformation mechanisms of AlCrFeCuNi [15] and $Al_{0.1}$CoCrFeNi [16] HEAs under uniaxial tension were investigated by MD simulations, and the evolution of dislocations and twins was particularly characterized. Rao et al. performed MD simulations of $Co_{30}Fe_{16.67}Ni_{36.67}Ti_{16.67}$ and $Co_{16.67}Fe_{36.67}Ni_{16.67}Ti_{30}$ alloys to study the mobility of a/2 < 110 > dislocations and a/2 < 111 > dislocations, respectively [17,18]. In HEAs, severe lattice distortion is a typical character, which plays an important role in the microstructures (such as stacking faults, dislocations, twins) and mechanical properties. As such, MD simulation is capable of modeling the atomic structures and would be an effective tool to investigate the severe lattice distortion. Nevertheless, there is still a lack of understanding of the effects of severe lattice distortion on twinning in HEAs.

In this work, MD simulations were employed to investigate the effect of alloying elements (or severe lattice distortion) on twin nucleation and migration in FCC $Al_{0.25}CoFeNiCu_{0.75}$ HEA. In particular, 9 compositions with an increasing alloying element number (from pure Ni, Ni–Cu, Ni–Cu–Fe, Ni–Cu–Fe–Co to Ni–Cu–Fe–Co–Al) were investigated. The remainder of this paper is organized as follows. The computational methods and models are introduced in Section 2. The main results are presented and discussed in Section 3. Finally, concluding remarks are made in Section 4.

2. Simulation methods

Here, the $Al_{0.25}CoFeNiCu_{0.75}$ alloy is chosen as a model HEA material, which has a single FCC solid solution phase with a lattice constant of $a = 3.5882$ Å [7]. To investigate the effects of different alloying elements on the twin nucleation and propagation, different atomistic simulation cells are constructed by sequentially adding the alloying elements (Cu, Fe, Co, Al) to a base pure Ni matrix according to the concentration of each element in the $Al_{0.25}CoFeNiCu_{0.75}$ HEA. Half the final concentration of each element is added each time and all alloying atoms were randomly populated in each simulation cell. Accordingly, a total of nine simulation cells representing nine different alloy compositions are modeled (named A0 through A8), as summarized in Table 1. It should be noted that in Table 1 the mole fraction (ratio) is transformed into atomic percentage for all the 9 compositions to clearly elucidate the concentration change. To account for the statistical variation in composition, three simulations were run for each alloy with the atoms having different random distributions in the simulation cell.

As showed in Ref. [7], alloy A8 has been experimentally investigated and shown to have an FCC lattice structure, while there are no experimental studies on alloys A1-A7. The phase stability can be quantitatively predicted by the mixing enthalpy, $\Delta H_{mix} = \sum_{i=1,j\neq i}^{n} 4\Delta H_{AB}^{mix} c_i c_j$, where ΔH_{AB}^{mix} is the enthalpy of mixing for a liquid binary alloy AB [19]. The valence electron concentration is $VEC = \sum_{i=1}^{n} ci(VEC)_i$, where $(VEC)_i$ is the valence electron concentration of the i^{th} element [20]. The misfit strain, δ, is computed as [21].

$$\delta = \sqrt{\sum_{i=1}^{N} c_i \left(1 - r_i / \left(\sum_{i=1}^{N} c_i r_i\right)\right)^2} \quad (1)$$

where c_i is the atom concentration and r_i is the atom radius of the i^{th} alloying element. The atom radiuses are 1.245 Å for Ni, 1.24 Å for Fe, 1.25 Å for Co, 1.28 Å for Cu, and 1.43 Å for Al atoms [6]. As shown in Refs. [20,22], a stable FCC solid solution phase is expected when $-22 \leq \Delta H_{mix} \leq 7$, $VEC \geq 8$ and $\delta \leq 6.6\%$. The theoretical calculations of ΔH_{mix}, VEC and δ are summarized in Table 2 for alloys A1-A8. It is observed that the computed values for ΔH_{mix}, VEC and δ indicate all these alloys should have a stable FCC crystal structure. In MD simulations, we also compared the lattice energies or atom potential energies of A8 HEA with FCC and BCC lattices. The mean atom potential energy of FCC lattice is −4.16134 eV, while that of BCC lattice is −4.16022 eV. It can be seen the FCC lattice has a lower energy and is stable. This agrees well with the experimental observations in Ref. [7].

All the current MD simulations are performed using the open source code LAMMPS [23]. The interatomic interactions are described by the embedded atomic method (EAM) potential for multiple alloying elements developed by Zhou et al. [24,25]. This EAM potential has been utilized recently to model Al-Co-Cr-Cu-Fe-Ni [26] and Co–Fe–Ni–Ti [17,18] HEA systems. All the simulations are performed at 0 K. Common neighbor analysis (CNA) [27] and centro-symmetric parameter (CSP) are computed to identify the local lattice structures and types of defects in a crystal. Finally, OVITO [28] is employed to visualize the lattice defects and microstructure evolution.

Table 1
Composition of the 9 nanopillars from pure Ni to $Al_{0.25}CoFeNiCu_{0.75}$ HEA (at. %). Here the mole ratio is transformed into atomic percentage for all the compositions.

Alloy composition	Name	Ni	Cu	Fe	Co	Al
Ni	A0	100	0	0	0	0
$Ni_{90.7}Cu_{9.3}$	A1	90.7	9.3	0	0	0
$Ni_{81.25}Cu_{18.75}$	A2	81.25	18.75	0	0	0
$Ni_{69}Cu_{18.75}Fe_{12.25}$	A3	69	18.75	12.25	0	0
$Ni_{56.25}Cu_{18.75}Fe_{25}$	A4	56.25	18.75	25	0	0
$Ni_{44}Cu_{18.75}Fe_{25}Co_{12.25}$	A5	44	18.75	25	12.25	0
$Ni_{31.25}Cu_{18.75}Fe_{25}Co_{25}$	A6	31.25	18.75	25	25	0
$Ni_{28.12}Cu_{18.75}Fe_{25}Co_{25}Al_{3.13}$	A7	28.12	18.75	25	25	3.13
$Ni_{25}Cu_{18.75}Fe_{25}Co_{25}Al_{6.25}$	A8	25	18.75	25	25	6.25

Table 2
Theoretically predicted mixing enthalpy, ΔH_{mix} (kJ/mol), valence electron concentration, VEC (e/a), and misfit strain δ (%) for all the compositions studied here.

Alloy#	A1	A2	A3	A4	A5	A6	A7	A8
ΔH_{mix}	1.35	2.44	2.59	3.00	3.31	3.63	1.86	0.27
VEC	10.09	10.19	9.94	9.69	9.57	9.44	9.22	9.00
δ	0.695	0.933	0.982	0.990	0.990	0.990	2.52	3.35

2.1. Nanopillar compression simulations

Nanopillar simulation cells are constructed for all the 9 different compositions. A schematic representation of a nanopillar simulation cell of the $Al_{0.25}CoFeNiCu_{0.75}$ HEA (case A8) is shown in Fig. 1(a). All simulated nanopillars are rectangular with edge lengths $l_X = l_Y = 30$ nm, and $l_Z = 100$ nm, in the three orthogonal directions $X = [100]$, $Y = [010]$, and $Z = [001]$, respectively. The total number of atoms in each simulation cell is ~7.76 million. Free surface boundary conditions are employed in the three directions. After atoms in each simulation cell are initialized, the simulation cell is energetically minimized by the conjugate gradient algorithm to obtain a stable single-phase structure.

A uniaxial compressive strain, ε_c, is then imposed on the top and bottom surfaces (in the Z-axis direction) at a strain rate of $10^8\ s^{-1}$ using the NVT ensemble and a time step of 0.001 Ps [29]. The strain is imposed by freezing all atoms in a 1 nm thick slab at the top and bottom of the simulation cell, then imposing opposite displacements on all atoms in the two surface slabs.

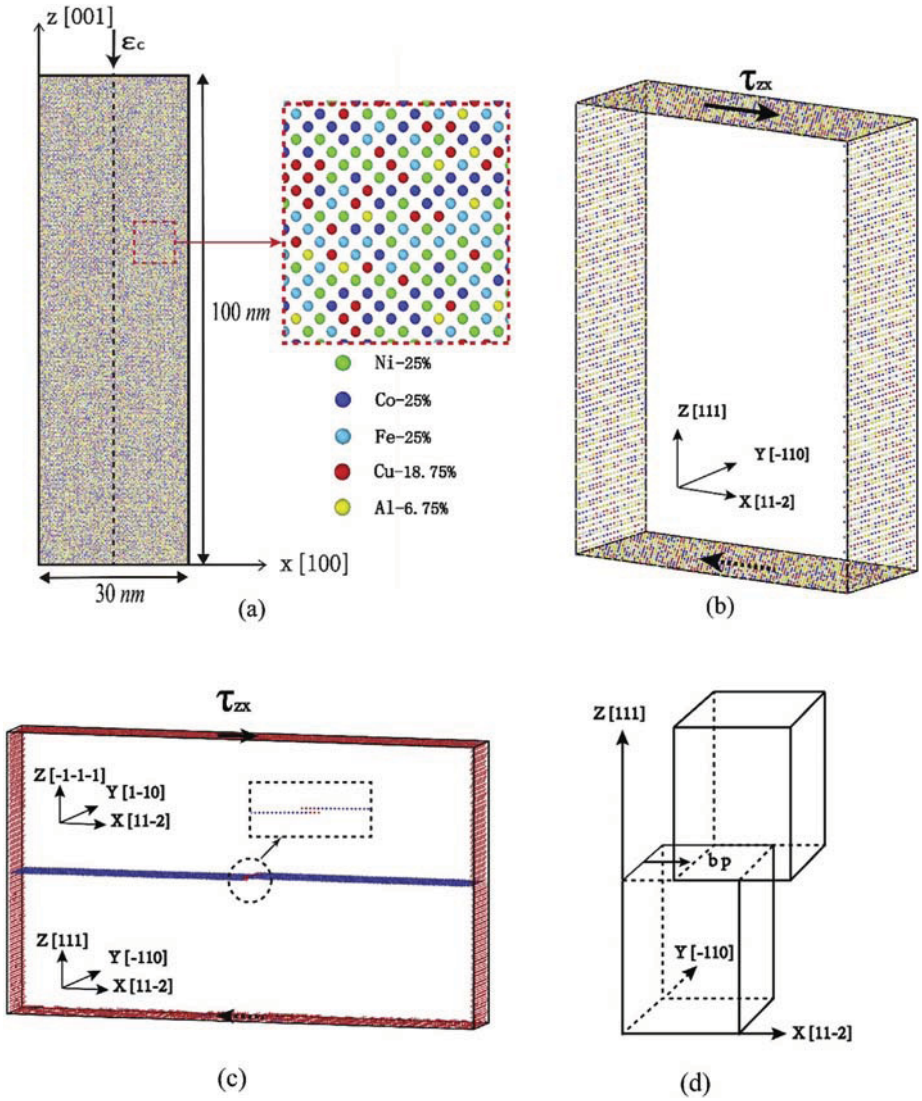

Fig. 1. (a) A schematic representation of the nanopillar simulation cell after energy minimization of the $Al_{0.25}CoFeNiCu_{0.75}$ HEA (case A8). (b) A schematic representation of a rectangular simulation cell of $Al_{0.25}CoFeNiCu_{0.75}$ HEA under the shear stress imposed along the $[11\bar{2}]$ direction for the calculation of the twin nucleation stress. Atoms in perfect lattice are not shown (i.e. only atoms on the free surfaces are shown). The atoms in (a) and (b) are colored by the atom type as indicated by the insert in (a). (c) A simulation cell showing a twin boundary with an initial twinning dislocation (see insert) on the twin boundary for the calculation of the twin migration stress. Atoms in perfect lattice are not shown. The red atoms on the cell boundary in (c) represent free surfaces, while the blue atoms represent a twin boundary at which red atoms are twinning dislocations. (d) A schematic of the simulations to calculate the GPFE. (For interpretation of the references to color in this figure legend, the reader is referred to the Web version of this article.)

2.2. Simulations of twin nucleation and migration stresses

To calculate the twin nucleation stress, the simulation cell shown in Fig. 1(b), with edge lengths $30\sqrt{1.5}a$, $10\sqrt{2}a$, and $30\sqrt{3}a$ in the three orthogonal crystallographic directions, $X = [11\bar{2}]$, $Y = [\bar{1}10]$, and $Z = [111]$, respectively is employed. . Periodic boundary conditions are employed in the $[\bar{1}10]$ direction, while free surface boundary conditions are imposed in the other two directions. A pure shear strain is imposed by freezing atoms in a 1 nm thick slab at the bottom of the simulation cell and imposing a constant velocity in the $X = [11\bar{2}]$ direction on all atoms in a 1 nm thick slab at the top of the simulation cell at a strain rate of $\dot{\varepsilon}_{zx} = 10^8 s^{-1}$ with the NVE ensemble [30].

Furthermore, the migration of a twin boundary is mediated by the glide of twinning dislocations on the twin boundary. Accordingly, the critical stress for twin migration is defined here as the critical resolved shear stress for the glide of a twinning dislocation. To compute this stress, the simulation cell shown in Fig. 1(c), with edge lengths $100\sqrt{3/2}$ a, $10\sqrt{2}a$, and $50\sqrt{3}a$, in the three orthogonal global X, Y, and Z directions respectively, is utilized. Periodic boundary conditions are employed along the global Y direction, while free surface boundary conditions are imposed along the other two directions. A twin boundary is introduced at the center of the simulation cell parallel to the global XY plane. The local lattice orientation above the twin boundary is $[11\bar{2}]$, $[1\bar{1}0]$, and $[\bar{1}\,\bar{1}\,\bar{1}]$, while below it is $[11\bar{2}]$, $[\bar{1}10]$, and $[111]$. A twinning dislocation parallel to the global Y direction having a Burgers vector $\boldsymbol{b}_t = a/6 < 112 >$ is then introduced on the twin boundary by transferring one half of the twin boundary to the neighboring atomic plane. A pure shear strain was then imposed parallel to the global X direction at a strain rate of $\dot{\varepsilon}_{zx} = 10^8 s^{-1}$ using the NVE ensemble.

2.3. Generalized planar fault energy (GPFE) calculations

The generalized planar fault energies (GPFE) of $< 112 > /\{111\}$ twins is calculated for all 9 compositions to quantify the effect of alloying on deformation twinning. For these calculations a rectangular simulation cell is utilized, with edge lengths $20\sqrt{3/2}$ a, $20\sqrt{2}a$, and

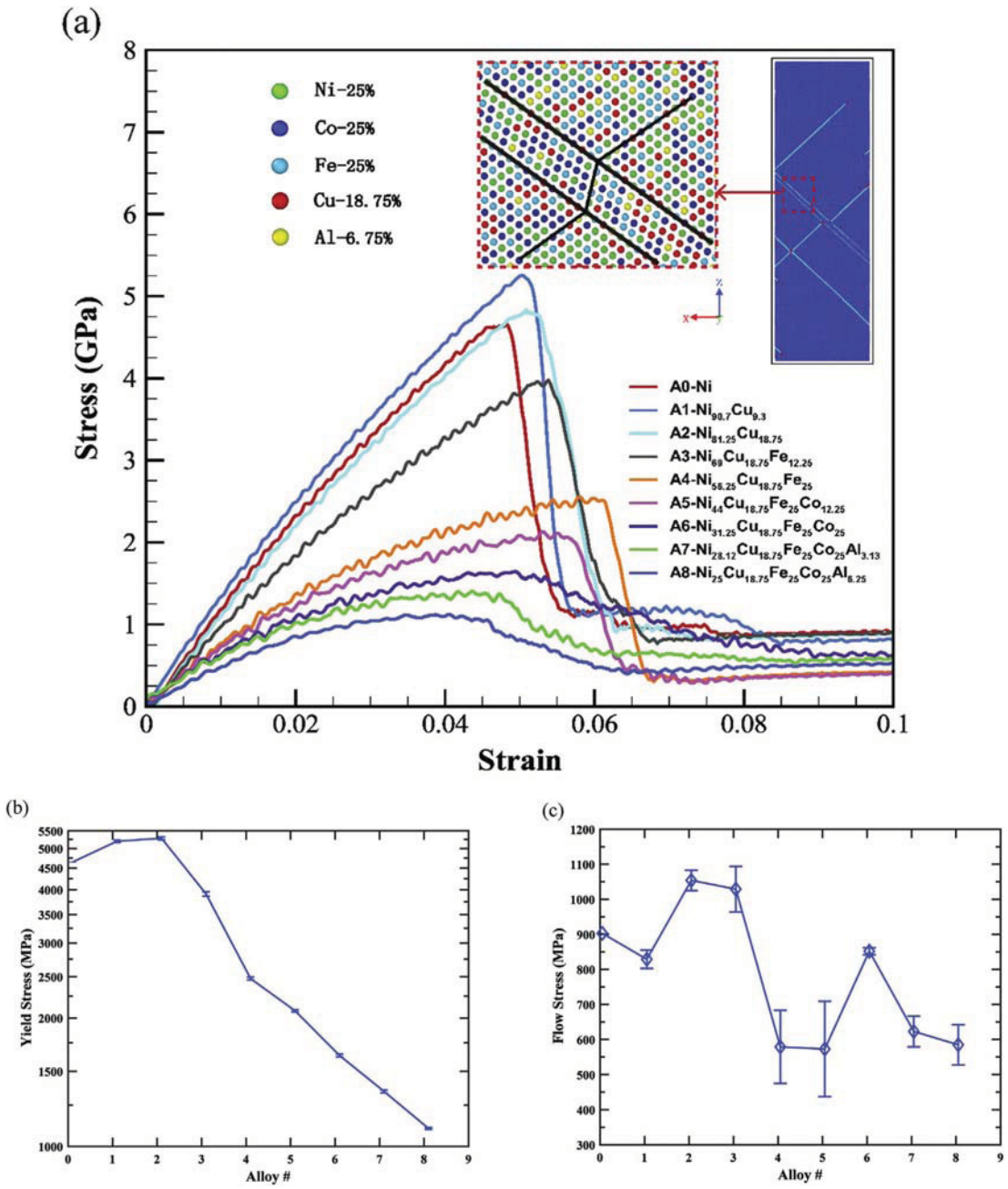

Fig. 2. (a) Stress-strain curves of the 9 nanopillars with different composition under uniaxial compression. The insert shows the twins in $Al_{0.25}CoFeNiCu_{0.75}$ HEA nanopillar. (b) Yield stresses and (c) flow stresses in the 9 nanopillars versus the alloy number. The horizonal axes show the alloy number.

$20\sqrt{3}a$ in the three orthogonal directions X = [11–2], Y = [−110] and Z = [111], respectively, as shown schematically in Fig. 1(d). Periodic boundary conditions are employed in the X and Y directions, while free surface boundary conditions are employed along the Z direction. The upper half of the simulation cell is then sheared relative to the lower-half along the twinning partial Burgers Vector, $\boldsymbol{b}_p$[31]. This shear process was repeated twice on neighboring {111} slip planes so as to mimic the nucleation of a twin embryo [32].

3. Results and discussions

3.1. Effects of alloying on twin nucleation and migration

The predicted stress-strain curves for nanopillar simulation cells under compression for the nine different compositions are shown in Fig. 2. For all compositions, the nanopillars deform elastically until the stresses reach a maximum, then the stresses drop considerably, followed by a steady plastic flow stage. Such a stress drop was frequently observed in nano-crystal experiments and is due to perfuse nucleation and multiplication of defects in a perfect nano-crystal after yield [33]. The insert in Fig. 1 shows the configuration of $Al_{0.25}CoFeNiCu_{0.75}$ HEA nanopillars at 3% strain, which indicates that plasticity is predominantly accommodated by nano-twinning. This is representative for the deformation mechanisms in all nine different compositions. Generally, twinning was not observed in nanopillar experiments of pure Ni. However, it is commonly observed in nanopillar MD simulations [34]. This discrepancy between MD simulations and experimental observations on nanopillar Ni single crystals is likely due to the higher strain rate in the MD simulations [35]. Nevertheless, even with such a discrepancy, the current results provide an avenue to quantify the effect of

alloying on twin nucleation and migration as will be discussed in the following.

Fig. 2(b) and (c) summarize the maximum (yield) stresses and the flow stresses of the nine different compositions simulated. It is observed that the maximum stresses of the Ni–Cu alloy are higher than that of pure Ni, then the maximum stress dramatically decreases with further addition of elements. In particular, the maximum stress of the pure Ni nanopillar is 4647 MPa, while that of $Al_{0.25}CoFeNiCu_{0.75}$ HEA is 1109 MPa. On the other hand, in Fig. 2(c), although the flow stress generally drops from ~1000 MPa to ~500 MPa, remarkable fluctuations are seen on the flow stress curve. This is a result of the twin-twin interactions. In some simulations only a single twin nucleates and propagates, so the stress is low. In other simulations, multiple twins nucleate and interact, so the predicted flow stress would be higher. Since no initial dislocations or twins were introduced in the MD simulations, the maximum strength is fully controlled by the nucleation of deformation twins. Therefore, the decrease of maximum strength here implies a decrease in the nucleation stress of twins due to alloying effects.

The twin nucleation stresses, defined here as the critical resolved shear stress (CRSS) for the nucleation of a $< 112 >/\{111\}$ twin embryo with a thickness of at least three atomic layers [36] nucleating from the free surface, are calculated for the 9 compositions using the simulation cells discussed in Section 2.2, and the results are summarized in Fig. 3(a). It is observed that the twin nucleation stress monotonically decreases with the addition of more alloying elements, indicating that deformation twinning is easier in HEAs as compared to pure Ni. In addition, the twin migration stresses, defined here as the critical resolved shear stress for the glide of a twinning dislocation on the twin boundary [37], are summarized in Fig. 3(b) for all the simulated compositions. The twin migration stress decreases as well with the addition of more alloying elements, indicating a solid solution effect on twin boundary migration.

3.2. Atomic stress and strain due to lattice distortion

As discussed earlier, the addition of more alloying elements in the HEAs leads to the decrease in twin nucleation and migration stresses. In order to further understand the origin of this effect, it is necessary to quantify the influence of lattice distortion in HEAs on deformation induced twinning. The HEAs have a single solid solution phase consisting of multiple principal elements, in which each atom has a random position within the lattice. Since different alloying atoms have different atom sizes, larger atoms are expected to induce a compressive stress state, while smaller ones induce a tensile stress state. Accordingly, each atom would experience a non-negligible strain and stress arising from the lattice distortion.

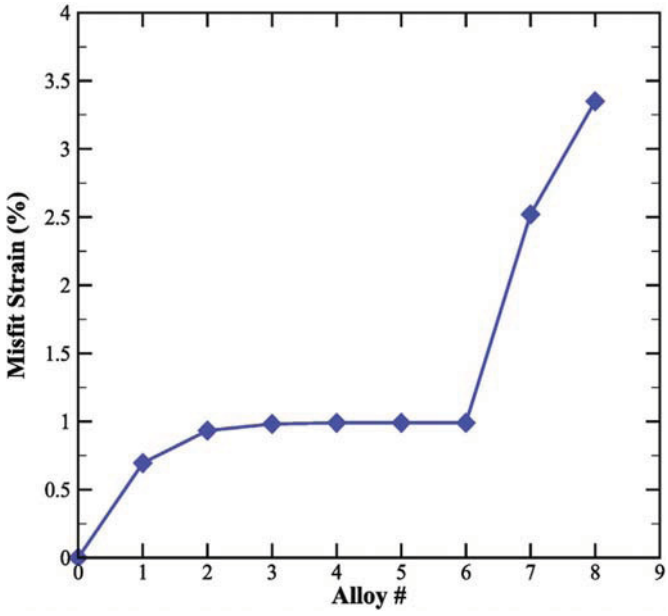

Fig. 4. Misfit strain for the different compositions modeled.

The average misfit strain is an indicator of the lattice distortion in the alloys, and is related to the difference between atom sizes [38]. The computed misfit strains from Eqn. (1) for all the considered compositions are shown in Fig. 4. It is observed that the misfit strain increases from 0 in pure Ni to 3.35% in the $Al_{0.25}CoFeNiCu_{0.75}$ HEA. In particular, the misfit strain increases to 0.98% when Cu atoms are added in the Ni matrix (*c.f.* alloys A1 and A2 in Fig. 4). However, the misfit strain increases weakly with the addition of Fe and Co atoms (*c.f.* alloys A3-A6 in Fig. 4) since their atom radiuses are nearly comparable to that of Ni atoms. Finally, the misfit strain pronouncedly increases up to 3.35% due to the addition of Al atoms, since Al atoms have the largest atom radius (*c.f.* alloys A7 and A8 in Fig. 4). It is worth noting that the maximum misfit strain is still smaller than the threshold value of 6.6% [39], indicating the crystal structure of these alloys is a stable disordered solid solution phase, although severe lattice distortion exists.

In order to measure the lattice distortion in the current MD simulations, the atomic von Mises strain and stress are computed for the undeformed nanopillars with different compositions. The von Mises strain of each atom is calculated as follows [40].

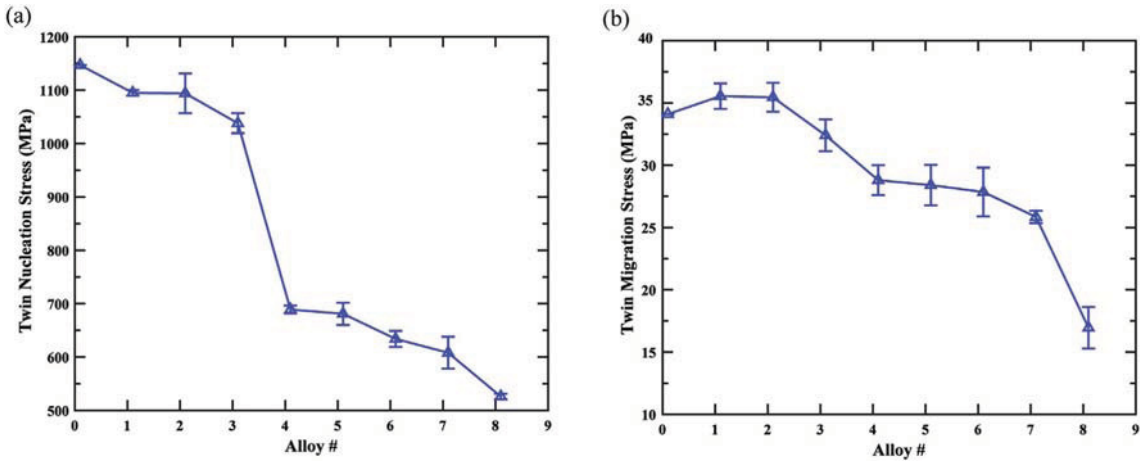

Fig. 3. The predicted (a) twin nucleation stresses and (b) migration stresses for the different alloy compositions studied here.

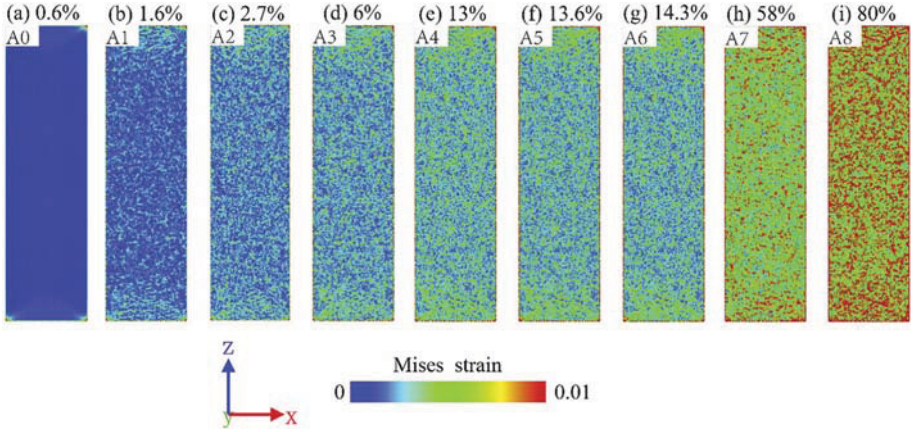

Fig. 5. Atomic strains in the 9 nanopillars modeled here: (a)–(i) are the atomic strain of A0-A8 alloys in sequence, and the percentage of atoms experiencing a strain larger than 0.005 are indicated.

$$\varepsilon_i^{\text{Mises}} = \sqrt{\varepsilon_{23}^2 + \varepsilon_{13}^2 + \varepsilon_{12}^2 + \frac{(\varepsilon_{22}-\varepsilon_{33})^2 + (\varepsilon_{11}-\varepsilon_{33})^2 + (\varepsilon_{11}-\varepsilon_{22})^2}{6}} \quad (2)$$

where ε_{jk} ($j, k = 1, 2$ and 3) is the component of the strain tensor at the ith atom. The atomic stains calculated using the OVITO software, are shown in Fig. 5 for all the different compositions modeled. It is observed that the atomic strain increases remarkably with the addition of alloying elements so the $Al_{0.25}CoFeNiCu_{0.75}$ HEA exhibits the highest atomic strain. In addition, the percentage of those atoms experiencing high strain (> 0.005) also increases with the addition of alloying elements but slowly for the A1-A6 alloys, where the Cu, Fe, Co atoms are added in sequence. On the other hand, the addition of Al atoms in the A7 and A8 alloys leads to a significant increase (from 14.3% to 80%) in the percentage of atoms experiencing high strains. The atomic strain agrees well with the calculation of the misfit strain shown in Fig. 4.

The atomic von Mises stresses for the different compositions are shown in Fig. 6, which are similar to those discussed for the atomic strains. The percentage of atoms experiencing high stress (> 0.5 MPa) increases as well but slowly for alloys A1-A6, where the Cu, Fe, Co atoms are sequentially added. On the other hand, the addition of Al atoms in alloys A7 and A8, leads to a significant increase (from 0.8% to 33%) in the percentage of atoms experiencing high stresses.

As is well known, the severe lattice distortion leads to the misfit strain, and thus the decrease in the twin nucleation stress. However, a long plateau is seen on the misfit strain in Fig. 5, while the nucleation stress is still decreasing in Fig. 4. This is because the misfit strain was calculated by the theoretical model based on the atom size difference only. This model fails to describe the specificity of different elements with same atom size, so does not well describe the lattice distortion. In order to see the actual lattice distortion in MD simulations, we can use the maximum atomic stress as an indicator, which directly controls the onset of twin nucleation. The maximum atomic stress is shown in Fig. 7. It is seen the maximum atomic stress increases monotonously with

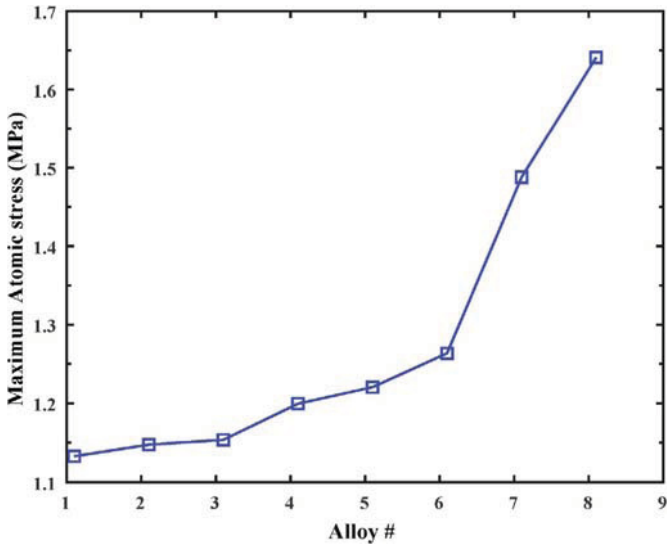

Fig. 7. Maximum atomic stress in the alloys modeled.

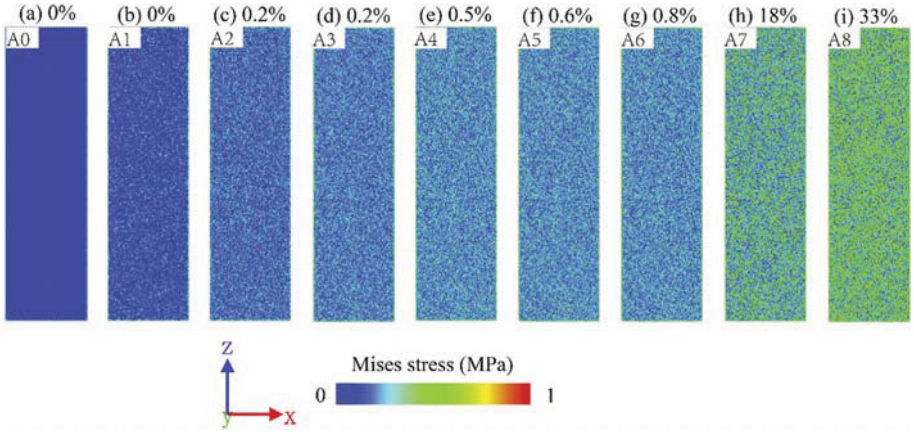

Fig. 6. Atomic stresses in the 9 nanopillars modeled here: (a)–(i) are the atomic stress of A0-A8 in sequence, in which the percentage of those atoms experiencing a stress larger than 0.5 MPa are indicated.

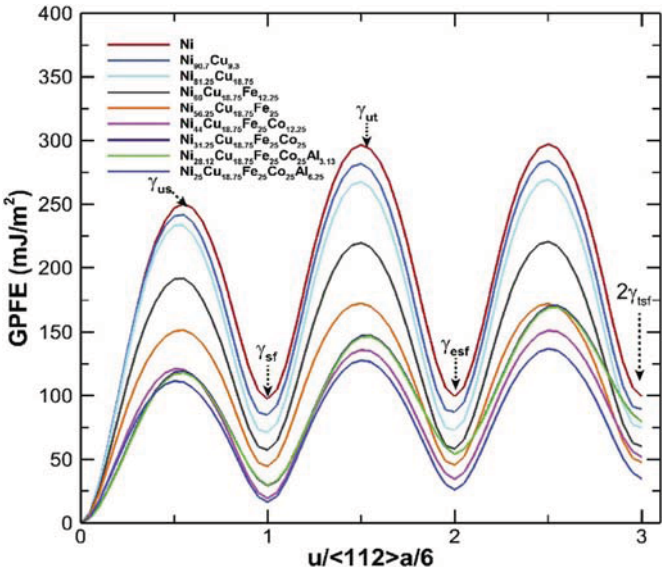

Fig. 8. The GPFE curves for the 9 compositions modeled.

increasing alloying element number, without the plateau in the misfit strain. The increase in the maximum atomic stress shows good agreement with the decrease in the twin nucleation stress and yielding stress.

3.3. Effect of alloying on the GPFE

Severe lattice distortion in HEAs not only induces atomic strains and stresses, but also dramatically changes interface energies, such as the stacking fault energy, twin boundary energy, and grain boundary energy [41]. The generalized stacking fault (GSF) surface can be used to characterize the interplanar energy, which is calculated by rigidly shifting the crystal along < 112 > direction on {111} slip plane for FCC metals [42]. The energy landscapes of deformation twinning and full dislocations obtained from GSF surface are referred to as GPFE curves and GSFE curves, respectively [43,44].

The calculated GPFE curves for the different compositions studied here are shown in Fig. 8. The first peak along the GPFE curves is the unstable stacking fault energy γ_{us}[45], which is the energy barrier for the nucleation of a leading dislocation partial. The subsequent valley is the < 112 > /6 stacking fault energy γ_{sf}. The second peak in Fig. 8 is associated with the successive shift on adjacent {111} plane, which is γ_{ut} known as the unstable twinning energy for the emission of a twinning partial. The following valley $\gamma_{esf}$is the extrinsic stacking fault energy [46], and the third valley is twice the energy of a twin boundary, $2\gamma_{tsf}$ [32].

The intrinsic material parameters calculated from the GPFE curves are summarized Table 3. It is clearly observed that all the intrinsic material parameters (γ_{us} , γ_{sf} , γ_{ut} , γ_{esf} and $2\gamma_{tsf}$) decrease with the successive addition of more alloying elements. For example, the stacking fault energy $\gamma_{sf} = 97\ \mathrm{mJ/m^2}$ for Ni, while for $Al_{0.25}CoFeNiCu_{0.75}$ $\gamma_{sf} = 16\ \mathrm{mJ/m^2}$. The low stacking fault energies agree well with the experimental results of $Al_{0.1}CoCrFeNi$ and FeCoNiCrMn HEAs, where the stacking fault energies are as low as ~ 6–21 $\mathrm{mJ/m^2}$ [10] and 21 $\mathrm{mJ/m^2}$ [47], respectively.

It is commonly suggested that the solid solute atoms in dilute solid solutions induce a local stress field due to lattice distortion, which acts as obstacles to dislocations and results in solid solution hardening [48]. However, in the HEAs, the lattice distortion induced by solid solute atoms in high concentration produces distortion energies such that to reduce the SFE. This further makes twin nucleation stress lower. Additionally, the decrease in flow stress could be correlated to the decrease in the twin boundary energy from 99 $\mathrm{mJ/m^2}$ in pure Ni, to 35 $\mathrm{mJ/m^2}$ in the $Al_{0.25}CoFeNiCu_{0.75}$ HEA, as shown in Table 3. The decrease in SFE and twin boundary energy indicates the improved ability to accommodate deformation by twins, which is in good agreement with the decrease in the twin nucleation and migration stress as discussed earlier in the nanopillar simulations.

Furthermore, the emission of a trailing partial dislocation for a full dislocation is determined by the energy barrier, $\gamma_{us} - \gamma_{sf}$ [45], while the nucleation of a twin partial for a full twin embryo depends on the energy barrier, $\gamma_{ut} - \gamma_{sf}$ [43]. Therefore the competition between full dislocation slip and deformation twinning depends on the relative energy barrier, $\delta_{us}^{ut} \equiv \gamma_{ut} - \gamma_{us}$ [49]. The computed values of δ_{us}^{ut} for the different compositions studied here are summarized in Table 3. It is observant that δ_{us}^{ut} decreases from 47 $\mathrm{mJ/m^2}$ for pure Ni to 17 $\mathrm{mJ/m^2}$ for $Al_{0.25}CoFeNiCu_{0.75}$ HEA. Since δ_{us}^{ut} is still greater than zero, the nucleation of twins is more difficult than the nucleation of a full dislocations (i.e. dislocation slip still dominates the plastic deformation in HEAs). This agrees well with experimental observations in bulk $Al_{0.1}CoCrFeNi$ [13] and CrMnFeCoNi [12] HEAs at low strain and room temperature. However, here in the nanopillars, only twinning deformation is observed rather than full dislocations, which is a direct result of the high strain rate in MD simulations [35].

4. Conclusions

In current work, molecular dynamics simulations were employed to model the compressive property of FCC $Al_{0.25}CoFeNiCu_{0.75}$ HEA nanopillars. To study the effects of alloying elements, the alloying elements (Cu, Fe, Co, Al) were sequentially added in pure Ni matrix based on Ni–Cu–Fe–Co–Al system. Simulation results suggest that the plastic deformation is mediated by deformation twinning in all nanopillars. However, the yield strength and flow stress decrease with the increase in the number of alloying elements. Then the twin nucleation stress and migration stress (Peierls stress of twinning dislocation) were calculated as well by MD simulations, which showed a drop as the addition of alloying elements.

As is well-known, the lattice distortion is severe in HEAs due to the difference in atom sizes of the alloying elements. To study the effect of

Table 3
Material parameters predicted from MD simulations. $\delta_{us}^{ut} = \gamma_{ut} - \gamma_{us}$ is the relative energy barrier. T_a is the twinnability, which is dependent on the dimensionless ratios of γ_{sf}/γ_{us} and γ_{us}/γ_{ut} .

Mater.	γ_{us}	γ_{sf}	γ_{ut}	γ_{esf}	$2\gamma_{tsf}$	γ_{sf}/γ_{us}	γ_{us}/γ_{ut}	δ_{us}^{ut}	T_a
A0: Ni	250	97	297	99	99	0.388	0.842	47	0.988
A1: $Ni_{90.7}Cu_{9.3}$	242	85	282	87	90	0.351	0.858	40	1.003
A2: $Ni_{81.25}Cu_{18.75}$	233	71	268	73	75	0.305	0.869	35	1.016
A3: $Ni_{69}Cu_{18.75}Fe_{12.25}$	191	57	220	58	60	0.299	0.868	29	1.017
A4: $Ni_{56.25}Cu_{18.75}Fe_{25}$	151	45	173	46	48	0.298	0.873	22	1.019
A5: $Ni_{44}Cu_{18.75}Fe_{25}Co_{12.25}$	121	19	136	35	52	0.157	0.890	15	1.049
A6: $Ni_{31.25}Cu_{18.75}Fe_{25}Co_{25}$	120	29	148	54	20	0.242	0.811	28	0.990
A7:$Ni_{28.12}Cu_{18.75}Fe_{25}Co_{25}Al_{3.13}$	118	30	146	55	80	0.254	0.808	28	0.987
A8: $Ni_{25}Cu_{18.75}Fe_{25}Co_{25}Al_{6.25}$	111	16	128	31	35	0.144	0.867	17	1.038

lattice distortion the atomic strain and stress were calculated for the 9 nanopillars studied, the atomic strain and percentage of those atoms experiencing high strain increase remarkably from pure Ni to $Al_{0.25}CoFeNiCu_{0.75}$ HEA, agreeing well with the prediction of severe lattice distortion. As a result of the atomic strain, the atomic stress and percentage of the atoms experiencing high stress also increase as the addition of more alloying elements.

The GPFE curves of the considered compositions were calculated to study the twinnability, which show that the stacking fault energy is 97 mJ/m^2 in Ni, while the energy in $Al_{0.25}CoFeNiCu_{0.75}$ HEA is as low as 16 mJ/m^2. The low stacking fault energies of HEAs are in line with that from the experimental observations. The relative energy barrier was calculated to determine the competition between full dislocation slip and deformation twinning, which suggests that dislocation slip still dominates the plastic deformation in HEAs. However, only twins in the nanopillars is observed rather than dislocations, which is due to the high strain rate used here.

Acknowledgements

The financial support from National Natural Science Foundation of China (U1730106, 11672193, 11672251) is acknowledged. JAE acknowledges support by the U.S. National Science Foundation (DMR-1807708).

References

[1] J.-W. Yeh, S.-K. Chen, S.-J. Lin, J.-Y. Gan, T.-S. Chin, T.-T. Shun, C.-H. Tsau, S.-Y. Chang, Nanostructured high-entropy alloys with multiple principal elements: novel alloy design concepts and outcomes, Adv. Eng. Mater. 6 (2004) 299–303.
[2] B. Cantor, I.T.H. Chang, P. Knight, A.J.B. Vincent, Microstructural development in equiatomic multicomponent alloys, Mater. Sci. Eng. A 375–377 (2004) 213–218.
[3] Y. Zhang, T. Zuo, Y. Cheng, P.K. Liaw, High-entropy alloys with high saturation magnetization, electrical resistivity, and malleability, Sci. Rep. 3 (2013) 1455.
[4] Y.F. Ye, Q. Wang, J. Lu, C.T. Liu, Y. Yang, High-entropy alloy: challenges and prospects, Mater. Today 19 (2016) 349–362, https://doi.org/10.1016/j.mattod.2015.11.026.
[5] Y. Zhang, T.T. Zuo, Z. Tang, M.C. Gao, K.A. Dahmen, P.K. Liaw, Z.P. Lu, Microstructures and properties of high-entropy alloys, Prog. Mater. Sci. 61 (2014) 1–93.
[6] C.-C. Tung, J.-W. Yeh, T.-T. Shun, S.-K. Chen, Y.-S. Huang, H.-C. Chen, On the elemental effect of AlCoCrCuFeNi high-entropy alloy system, Mater. Lett. 61 (2007) 1–5.
[7] X. Chen, L. Yan, S. Karnati, Y. Zhang, F. Liou, Fabrication and characterization of AlxCoFeNiCu1 − x high entropy alloys by laser metal deposition, Coat. World 7 (2017) 47.
[8] Z. Li, K.G. Pradeep, Y. Deng, D. Raabe, C.C. Tasan, Metastable high-entropy dual-phase alloys overcome the strength–ductility trade-off, Nature 534 (2016) 227–230, https://doi.org/10.1038/nature17981.
[9] C.-J. Tong, M.-R. Chen, J.-W. Yeh, S.-J. Lin, S.-K. Chen, T.-T. Shun, S.-Y. Chang, Mechanical performance of the Al x CoCrCuFeNi high-entropy alloy system with multiprincipal elements, Metall. Mater. Trans. A 36 (2005) 1263–1271.
[10] C.-W. Tsai, M.-H. Tsai, J.-W. Yeh, C.-C. Yang, Effect of temperature on mechanical properties of Al0.5CoCrCuFeNi wrought alloy, J. Alloy. Comp. 490 (2010) 160–165.
[11] B. Gludovatz, A. Hohenwarter, D. Catoor, E.H. Chang, E.P. George, R.O. Ritchie, A fracture-resistant high-entropy alloy for cryogenic applications, Science 345 (2014) 1153–1158.
[12] G. Laplanche, A. Kostka, C. Reinhart, J. Hunfeld, G. Eggeler, E.P. George, Reasons for the superior mechanical properties of medium-entropy CrCoNi compared to high-entropy CrMnFeCoNi, Acta Mater. 128 (2017) 292–303.
[13] P.F. Yu, H. Cheng, L.J. Zhang, H. Zhang, Q. Jing, M.Z. Ma, P.K. Liaw, G. Li, R.P. Liu, Effects of high pressure torsion on microstructures and properties of an Al 0.1 CoCrFeNi high-entropy alloy, Mater. Sci. Eng. A 655 (2016) 283–291.
[14] H. Huang, H. Van Swygenhoven, Atomistic simulations of mechanics of nanostructures, MRS Bull. 34 (3) (2011) 160–166.
[15] J. Li, Q. Fang, B. Liu, Y. Liu, Y. Liu, Mechanical behaviors of AlCrFeCuNi high-entropy alloys under uniaxial tension via molecular dynamics simulation, RSC Adv. 6 (2016) 76409–76419.
[16] A. Sharma, G. Balasubramanian, Dislocation dynamics in Al0.1CoCrFeNi high-entropy alloy under tensile loading, Intermetallics 91 (2017) 31–34.
[17] S.I. Rao, C. Woodward, T.A. Parthasarathy, O. Senkov, Atomistic simulations of dislocation behavior in a model FCC multicomponent concentrated solid solution alloy, Acta Mater. 134 (2017) 188–194.
[18] S.I. Rao, C. Varvenne, C. Woodward, T.A. Parthasarathy, D. Miracle, O.N. Senkov, W.A. Curtin, Atomistic simulations of dislocations in a model BCC multicomponent concentrated solid solution alloy, Acta Mater. 125 (2017) 311–320.
[19] Y. Zhang, Y.J. Zhou, J.P. Lin, G.L. Chen, P.K. Liaw, Solid-solution phase formation rules for multi-component alloys, Adv. Eng. Mater. 10 (2008) 534–538.
[20] S. Guo, C. Ng, J. Lu, C.T. Liu, Effect of valence electron concentration on stability of fcc or bcc phase in high entropy alloys, J. Appl. Phys. 109 (2011) 103505.
[21] L.R. Owen, E.J. Pickering, H.Y. Playford, H.J. Stone, M.G. Tucker, N.G. Jones, An assessment of the lattice strain in the CrMnFeCoNi high-entropy alloy, Acta Mater. 122 (2017) 11–18.
[22] F. Tian, L.K. Varga, N. Chen, J. Shen, L. Vitos, Empirical design of single phase high-entropy alloys with high hardness, Intermetallics 58 (2015) 1–6.
[23] S. Plimpton, Fast parallel algorithms for short-range molecular dynamics, J. Comput. Phys. 117 (1) (1995) 1–19.
[24] X.W. Zhou, H.N.G. Wadley, R.A. Johnson, D.J. Larson, N. Tabat, A. Cerezo, A.K. Petford-Long, G.D.W. Smith, P.H. Clifton, R.L. Martens, T.F. Kelly, Atomic scale structure of sputtered metal multilayers, Acta Mater. 49 (2001) 4005–4015.
[25] X.W. Zhou, R.A. Johnson, H.N.G. Wadley, Misfit-energy-increasing dislocations in vapor-deposited CoFe/NiFe multilayers, Phys. Rev. B 69 (14) (2004) 144113.
[26] L. Xie, P. Brault, A.-L. Thomann, X. Yang, Y. Zhang, G. Shang, Molecular dynamics simulation of Al–Co–Cr–Cu–Fe–Ni high entropy alloy thin film growth, Intermetallics 68 (2016) 78–86.
[27] D. Faken, H. Jónsson, Systematic analysis of local atomic structure combined with 3D computer graphics, Comput. Mater. Sci. 2 (2) (1994) 279–286.
[28] S. Alexander, Visualization and analysis of atomistic simulation data with OVITO–the Open Visualization Tool, Model. Simul. Mater. Sci. Eng. 18 (1) (2010) 015012.
[29] H. Fan, J.A. El-Awady, Molecular dynamics simulations of orientation effects during tension, compression, and bending deformations of magnesium nanocrystals, J. Appl. Mech. 82 (10) (2015) 101006-101006-11.
[30] H. Fan, Q. Wang, X. Tian, J.A. El-Awady, Temperature effects on the mobility of pyramidal < c + a > dislocations in magnesium, Scr. Mater. 127 (2017) 68–71.
[31] S. Kibey, J.B. Liu, D.D. Johnson, H. Sehitoglu, Generalized planar fault energies and twinning in Cu–Al alloys, Appl. Phys. Lett. 89 (2006) 191911.
[32] S. Mahajan, G.Y. Chin, Formation of deformation twins in f.c.c. crystals, Acta Metall. 21 (10) (1973) 1353–1363.
[33] A. Kunz, S. Pathak, J.R. Greer, Size effects in Al nanopillars: single crystalline vs. bicrystalline, Acta Mater. 59 (11) (2011) 4416–4424.
[34] X. Li, W. Yang, Size dependence of dislocation-mediated plasticity in Ni single crystals: molecular dynamics simulations, J. Nanomater. 2009 (2009) 1–10.
[35] L.A. Zepeda-Ruiz, A. Stukowski, T. Oppelstrup, V.V. Bulatov, Probing the limits of metal plasticity with molecular, Nature 550 (2017) 492–495.
[36] S. Kibey, J.B. Liu, D.D. Johnson, H. Sehitoglu, Predicting twinning stress in fcc metals: linking twin-energy pathways to twin nucleation, Acta Mater. 55 (2007) 6843–6851.
[37] F.C. Frank, LXXXIII. Crystal dislocations.—elementary concepts and definitions, the london, edinburgh, and dublin, Philosophical Magazine and Journal of Science 42 (331) (1951) 809–819.
[38] P.-K. Huang, J.-W. Yeh, Inhibition of grain coarsening up to 1000°C in (AlCrNbSiTiV)N superhard coatings, Scr. Mater. 62 (2) (2010) 105–108.
[39] X. Yang, Y. Zhang, Prediction of high-entropy stabilized solid-solution in multi-component alloys, Mater. Chem. Phys. 132 (2) (2012) 233–238.
[40] F. Shimizu, S. Ogata, J. Li, Theory of shear banding in metallic glasses and molecular dynamics calculations, Mater. Trans. 48 (11) (2007) 2923–2927.
[41] M.C. Gao, J.-W. Yeh, P.K. Liaw, Yong Zhang, High-entropy Alloys: Fundamentals and Applications, Springer, Cham, Switzerland, 2016.
[42] V. Vítek, Intrinsic stacking faults in body-centred cubic crystals, Philos. Mag.: A Journal of Theoretical Experimental and Applied Physics 18 (154) (1968) 773–786.
[43] H. Van Swygenhoven, P.M. Derlet, A.G. Frøseth, Stacking fault energies and slip in nanocrystalline metals, Nat. Mater. 3 (2004) 399.
[44] A.Z. Jonathan, G. Huajian, F.A. Farid, Generalized stacking fault energies for embedded atom FCC metals, Model. Simul. Mater. Sci. Eng. 8 (2) (2000) 103.
[45] J.R. Rice, Dislocation nucleation from a crack tip: an analysis based on the Peierls concept, J. Mech. Phys. Solids 40 (2) (1992) 239–271.
[46] E.B. Tadmor, N. Bernstein, A first-principles measure for the twinnability of FCC metals, J. Mech. Phys. Solids 52 (11) (2004) 2507–2519.
[47] A.J. Zaddach, C. Niu, C.C. Koch, D.L. Irving, Mechanical properties and stacking fault energies of NiFeCrCoMn high-entropy alloy, JOM 65 (2013) 1780–1789.
[48] G.P.M. Leyson, W.A. Curtin, L.G. Hector Jr., C.F. Woodward, Quantitative prediction of solute strengthening in aluminium alloys, Nat. Mater. 9 (2010) 750.
[49] D.J. Siegel, Generalized stacking fault energies, ductilities, and twinnabilities of Ni and selected Ni alloys, Appl. Phys. Lett. 87 (12) (2005) 121901.